REST HF-9 test case: Large-Eddy Simulation of DLR's BKD configuration

Thomas Schmitt, Gabriel Staffelbach

DOI: ADD DOINUMBER HERE

REST HF-9 test case: Large-Eddy Simulation of DLR's BKD configuration

Thomas Schmitt[1†], *Gabriel Staffelbach*[2]
[1]*Laboratoire EM2C, CNRS, CentraleSupélec, Université Paris-Saclay,*
3, rue Joliot Curie, 91192 Gif-sur-Yvette cedex, France
[2]*Centre Européen de Recherche et de Formation Avancée en Calcul Scientifique (CERFACS),*
42, Avenue Gaspard Coriolis, 31057 Toulouse Cedex 01, France
[†]Corresponding author (thomas.schmitt@centralesupelec.fr)

Abstract

The results from the large-eddy simulations of BKD bench from DLR (Gröning et al., JPP, 2016) are shown in this contribution. The code is applied to two operating points of the hydrogen ramping experiment from Gröning et al. (CEAS space journal, 2016). The solver retrieves the dominant unstable modes that are observed experimentally. However, the grid resolution is found to have a major impact on the prediction of the dominant mode. While average quantities are weakly impacted by a coarsening of the mesh, the final prediction of the mode growth and its limit cycle can be completely modified.

1. Introduction

Combustion instability arises from the resonant coupling between the unsteady heat release rate of the flame and the acoustic eigenmodes of the system. High-frequency instabilities, corresponding to the coupling with a transverse acoustic mode of the combustion chamber, are the most dangerous ones and remain an issue during the development of liquid rocket engines, because of the curent inability to accurately predict their occurence. The objective of this work is the evaluation of Large-Eddy Simulation (LES) for the prediction of combustion instabilities occurring naturally in a cryogenic rocket engine combustion chamber. This study concerns the numerical simulation of the BKD bench of the DLR.[1,2] Equipped with 42 injectors, this configuration is similar to a small rocket engine. Depending on the injection conditions, the engine can be stable or unstable. In the first studies using LES,[3,4] instability did not appear naturally, probably due to the use of robust and thus more dissipative schemes. The mesh used was also poorly resolved. More recently, a natural transition between stable and unstable cases has been captured,[5] but not for the proper injection conditions. Again, the limited grid resolution as well as the impact of the walls treatment in the injector may explain this result. The ability of LES to properly retrieve the experimental observations is then not demonstrated at the moment. In particular, the impact of the grid resolution on the stability prediction has not been studied. This aspect is discussed in this paper.

The numerical framework is first presented in Sec. 2. The cases selected for the simulations and the grids are then discussed in Sec. 3. The influence of the grid resolution on the flow and stability prediction is then discussed in Sec. 4 for one the selected operating point. A second case, with a different natural instability is presented in Sec. 5.

2. Governing equations, models and numerics

The Large-Eddy Simulation (LES) approach depicted in Schmitt[6] is used in this work. It is briefly reminded here. It relies on the Soave-Redlich-Kwong (SRK) cubic equation of state,[7] used for a consistent derivation of all thermodynamic coefficients and functions.[8] The subgrid-scale (SGS) stress tensor is modeled with the WALE model,[9] with turbulent Prandtl and Schmidt numbers set to 0.6. Its Taylor-Galerkin weighted residual central distribution scheme, called TTGC, is third-order in time and space.[10] Boundaries are treated with the characteristic wave decomposition method NSCBC derived for non-ideal thermodynamics.[11] Chemical conversion is handled using an equilibrium chemistry model which accounts for the following species: H2, O2 , H2O and OH in order to properly calculate the burnt gas temperature. Equilibrium reference mass fractions are tabulated in terms of the mixture fraction and its variance, both transported during the simulations. The species source terms and heat release rate are then computed following the relaxation method described in Schmitt.[6]

3. Computational domain and simulated cases

3.1 Experimental configurations

The BKD experiment[1,2] is operated at the European Research and Technology Test Facility P8 for cryogenic rocket engines at DLR Lampoldshausen is a sub-scale thrust chamber featuring 42 H_2/O_2 coaxial injectors (Fig. 1a). This configuration has the particularity of featuring self-excited combustion instabilities depending on the injection conditions (Fig. 1b). The chamber is instrumented with a high frequency measurement ring including 2 dynamic pressure sensors, located at 5 mm from the injection plan. The chamber walls are water-cooled to limit their maximum temperature and heat loss measurements are available. The length and the radius of the chamber are of the order of 100 mm, while coaxial injectors features characteristic diameters representative of liquid rocket engines (o(10 mm)).

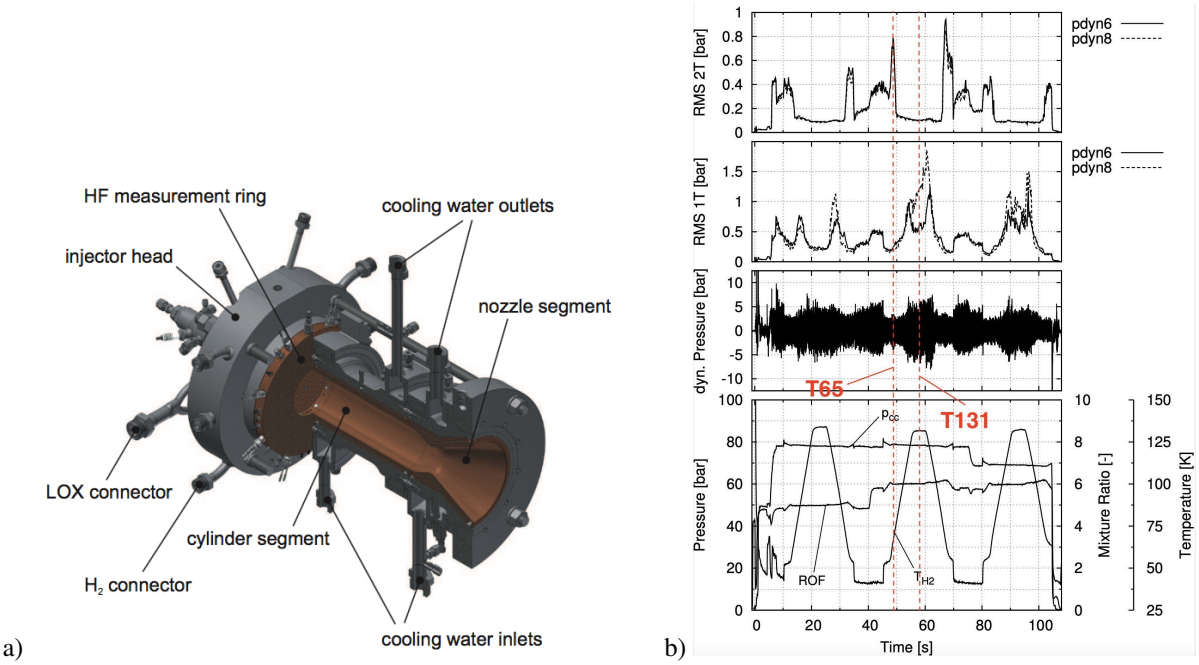

Figure 1: (a) Sketch of the BKD chamber[2] (b) Experimental results during ramp tests,[2] where hydrogen temperature is slowly changed. Gliding RMS calculation of the dynamic pressure sensor signals in the chamber (5 mm from injection plan) for the 1T and 2T modes, dynamic pressure sensor signal in chamber (5 mm from injection plan) and injection conditions.

In this study, we concentrate on the influence of hydrogen temperature injection on the thermo-acoustic stability of the chamber.[2] All the other injection characteristics (hydrogen and oxygen mass flow rates, oxygen temperature) are kept unchanged during the simulations. Injection conditions for the two cases of interest are shown in Tab. 1. The chamber pressure for both cases is close to 80 bar. Oxygen is transcritical (ρ_{LOx} = 1100 kg m^{-3}) and injected at low velocity (O(10 m s^{-1})), while hydrogen is supercritical (ρ_{H_2} = 29 kg m^{-3}) and injected at high velocity (O(100 m s^{-1})). The two cases retained for the simulations are represented in Fig. 1b. For case T65, the second transverse (2T) chamber acoustic mode dominates, while case T131 presents dominant fluctuations of the 1T mode of the chamber.

Case	$\dot{m}_{LOx}$ [kg/s]	$\dot{m}_{H_2}$ [kg/s]	T_{LOx} [K]	T_{H_2} [K]	Exp. behaviour
T65	5.8	0.97	107.6	65.0	Stable 1T mode, excited 2T mode
T131	5.8	0.97	107.6	131.7	Excited 1T mode, stable 2T mode

Table 1: Injection conditions for the two selected cases of the BKD experimental setup.[2]

3.2 Computational domain and boundary conditions

The computational domain is shown in Fig. 2 and corresponds to the experimental chamber, including the hydrogen and oxygen domes and feeding lines. In order to properly represent the outlet flow and acoustic impedance, the outlet nozzle is also simulated. All the solid boundaries are treated with adiabatic slip wall-law[12] and iso-thermal (500 K) wall-law are used at the chamber walls to account for water cooling. Oxygen and hydrogen are injected in the domes using non-reflecting boundary conditions with mass flow rates and temperatures imposed. As the nozzle is choked, nothing is imposed at outlet.

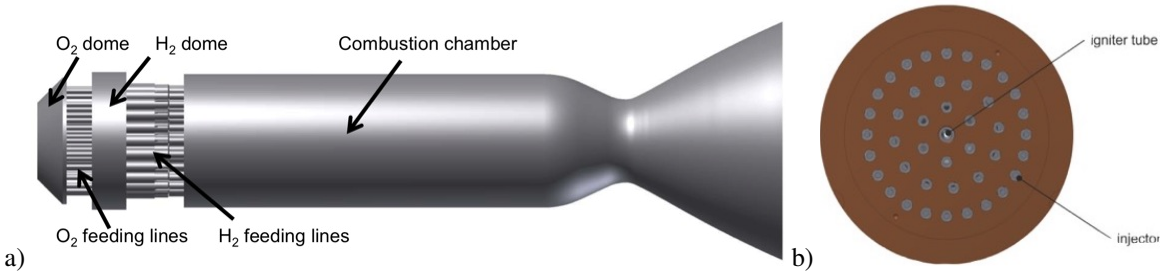

Figure 2: (a) Sketch of the full computational domain. (b) Injection plan featuring 42 injectors.

Because of accuracy limitations with the SRK equation of state, the oxygen injection temperature has been adjusted to match the experimental LOx sound speed. It is then changed from 107.6 K to 92 K. While this modification has a limited impact on density and energy, it importantly modifies the sound speed by more than 10 %. Accurately predicting the sound speed in the LOx pipes and dome is of importance to properly represent the coupling between the chamber and the feeding lines.

3.3 Meshes

Three different grid are used in this study to assess the influence of the grid resolution on the simulation results. An adaptative mesh refinement technique is applied in this work. The grid is refined in regions where the flow is poorly resolved, based on a sensor build on the Laplacian of the velocity, heat release and sound speed, computed from averaged solutions. The initial and coarser mesh is referenced as M0. Meshes M1 and M2 correspond to one and two iterations of refinement, respectively. Between each iteration, the grid characteristic cell size is divided at maximum by a factor 2 depending on the sensor value. Mesh M0 is poorly resolved in the injector exit region, with only 3 cells in the hydrogen injector and 10 cells in the oxygen stream. This mesh is thus highly computationally efficient but is expected to be weakly accurate in this region of the domain. It is found that the successive refinements essentially occur in the injector and in the recess. Mesh M2 is descritized with 23 cells in the O2 stream and 12 cells in the H2 injector. Detail of the meshes and their respective computational cost are given in Tab. 2.

Mesh	Nb of cells	Nb of points	CPU cost for 10 ms [kh]
M0	79.10^6	14.10^6	250
M1	258.10^6	45.10^6	1 500
M2	$1\,000.10^6$	174.10^6	20 000

Table 2: Detail of the three meshes and their respective cost.

An illustration of the flow obtained with mesh M2 for case T131 is offered in Fig. 3. The cold inner oxygen flows, surrounded by turbulent diffusion flames, penetrates up to one third of the chamber length. The hot gases then mix up to the outlet nozzle.

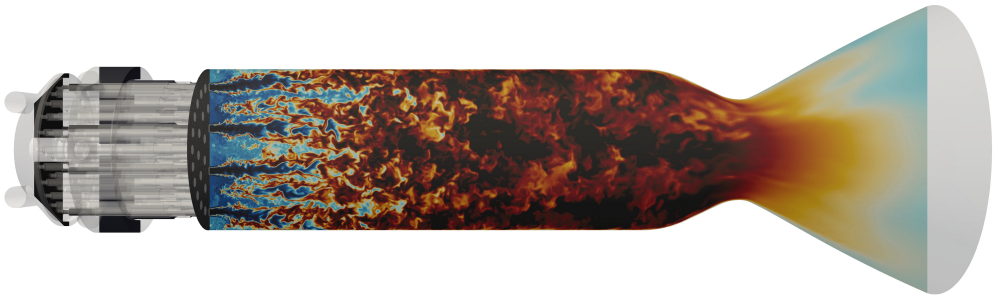

Figure 3: Longitudinal slice of instantaneous temperature between 92 and 3 600 K for case T131.

4. Impact of the mesh resolution on case T131

The influence of the grid resolution is first analyzed in Sec. 4.1 and 4.2 in terms of mean quantities of interest: temperature field, pressure loss and heat fluxes. The pressure dynamics and flame response to pressure perturbation is then discussed in Sec. 4.3.

4.1 Mean fields in the chamber

The mean fields for the three cases M0, M1 and M2 are now compared plotting mean radial profiles of temperature in the chamber in Fig. 4 for different axial location (x is the distance to the injection plan). The three grids show qualitatively similar results both in terms of mean and rms values in the chamber. However, for x=0 mm (at the injector exit), the profile is found to be highly dependent of the resolution. A mesh convergence study performed on a single injector configuration (not shown here) showed that M2 is actually virtually at convergence. This suggests that the grid refinement is not suffisent in this region for M0 and M1, however the weak dependance on the grid resolution for the prediction of the flame length and flow distribution in the chamber is noteworthy given the limited CPU cost of the coarser grid.

4.2 Pressure loss and heat fluxes at chamber walls

The pressure loss between the domes and the chamber is given in Tab. 3 for each cases. There is almost no impact of the mesh refinement on the pressure loss between the hydrogen dome and the chamber, while the coarse grid shows a larger pressure loss between the oxygen dome and the chamber than the two other grids. However, the difference remains limited and the three grids seem able to provide a satisfactory approximation of the pressure loss between the chamber and the domes. Moreover, the pressure in the chamber is in good agreement with the experimental measurements (78.5 bar in Fig. 4 in Gröning et al.[2]).

Case	P_{ch} [bar]	P_{O2} [bar]	Δ_{O2-ch}	P_{H2} [bar]	Δ_{H2-ch} [bar]
M0	78.7	91.2	12.5	105.8	27.1
M1	79.0	89.7	10.7	104.8	25.8
M2	79.3	89.5	10.2	103.9	24.6

Table 3: Case T131. Mean pressure in the oxygen dome (P_{O2}), in the hydrogen dome (P_{H2}) and in the chamber P_{ch}. Δ_{O2-ch} and Δ_{H2-ch} are the pressure loss between the oxygen dome and the chamber and the hydrogen dome and the chamber, respectively.

Finally, the impact of the grid on the heat loss through the chamber walls and the nozzle walls is detailed in Tab. 4. It is found that the three grids lead to similar prediction of the flux, all close to the experimental measurements.[2]

4.3 Pressure dynamics

The dynamical behavior of the system is now studied in terms of pressure Power Spectral Density (PSD). Each PSD is computed using 5 ms of temporal signal and is built from the average of 8 PSD computed with probes located at

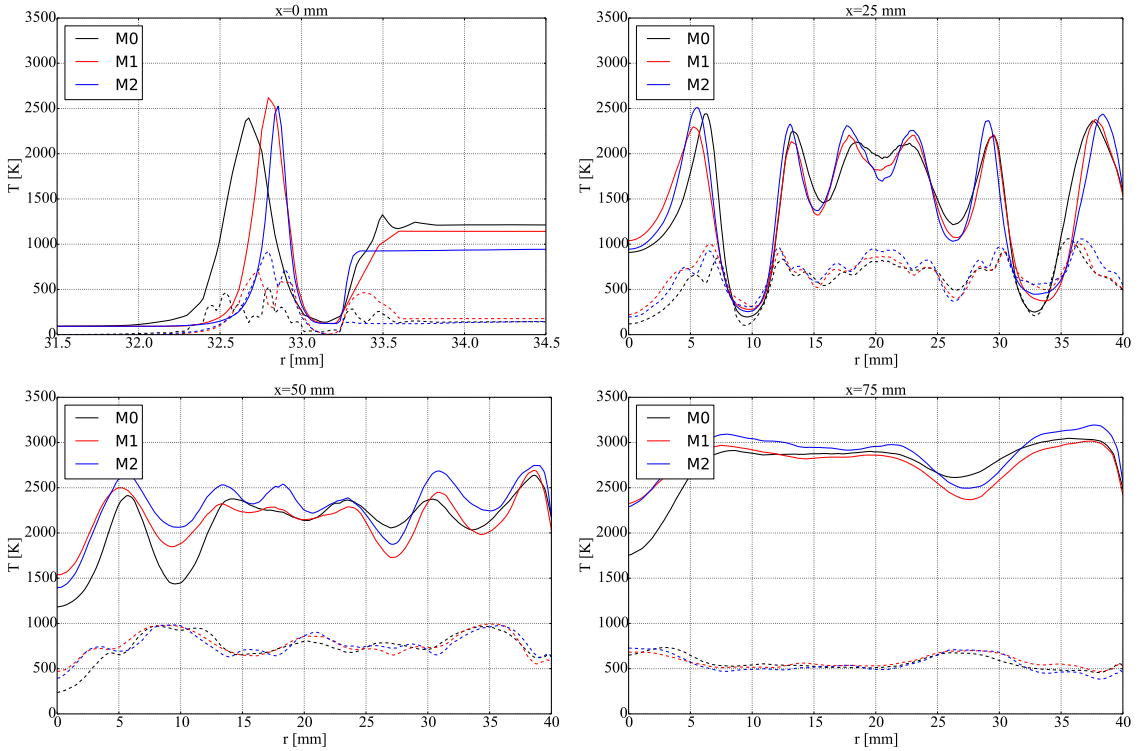

Figure 4: Case T131. Radial profiles of temperature for case M0, M1 and M2. − mean profiles, −− rms profiles.

Case	M0	M1	M2	Exp.
Chamber - Nozzle heat-flux [MW]	3.15	3.11	3.15	≈3.2

Table 4: Case T131. Heat flux through the chamber walls and the nozzle segment.

5 mm from the faceplate, along the chamber walls (positioned as in the experiment). Each cases now show a totally different dynamical behavior. The PSD for mesh M0 is dominated by a high amplitude 2T mode, while the 1T mode is not present. The latter is importantly increased has the grid is refined towards M1. In the meantime, the 2T mode is strongly diminished. Finally, M2 features a dominant 1T mode and a weakly excited 2T mode. This last behavior is in agreement with the experimental observations (Fig. 1b).

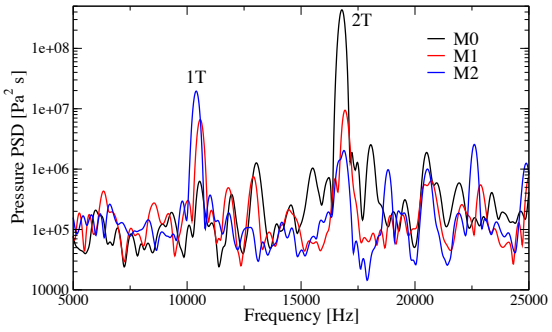

a)

Figure 5: Case T131. Power spectral density of pressure in (a) the chamber and (b) the LOx post for cases M0, M1 and M2. A Welch's method with 1 block is used, df=200 Hz, the last 5 ms are used for each case.

The mode frequencies, obtained from the PSD in Fig. 5, are compared with the experimental measurements from Gröning et al.[2] in Tab. 5. As for the mean quantities, the three meshes lead to similar frequencies, in reasonable

agreement with the experimental measurements, even though the 2T mode frequency is slightly under-predicted. The variations between the 3 cases should be analyzed with caution, given the limited frequency resolution of the PSD (200 Hz). Finally, the modes rms are computed from the PSD shown in Fig. 5 and are given in Tab. 5. As observed previously, there is a strong decrease of the 2T mode amplitude as the mesh is refined. On the contrary, 1T mode amplitude increases with the grid refinement. The 1T mode amplitudes on meshes M1 and M2 have not reach their limit cycle in the simulations, because of CPU requirement to compute the needed physical time. There are thus expected to be higher than the value given here. However, the results obtained with the finest grid are in agreement with the experimental observations: the 1T mode is excited, while the 2T mode is virtually stable.

Case	M0	M1	M2	Experiments[2]
1T mode freq.	10 550 Hz	10 600 Hz	10 400 Hz	10 500 Hz
1T mode rms.	0.22 bar	> 0.50 bar	> 0.79 bar	> 1.2 bar
2T mode freq.	16 850 Hz	16 900 Hz	16 900 Hz	17 150 Hz
2T mode rms.	3.60 bar	0.57 bar	0.32 bar	≈ 0.1 bar

Table 5: Case T131. Frequency of modes 1T and 2T in the chamber for cases M0, M1 and M2.

Finally a comparison of the flame response to pressure perturbations with the experimental measurements is offered in Fig. 6. Note that this experimental measurement have been produced on a slightly different operating point, with the same mass flow rates but a lower injection temperature for hydrogen (95 K instead of 131 K), namely LP4 operating point.[13] This experimental case has a similar behavior than case T131 and is also unstable for the 1T mode. It is then used here for a qualitative comparison with the numerical simulation. The histogram on the left of Fig. 6 presents the phase shift between the pressure and the heat release rate from LES. Histogram on the right of Fig. 6 shows the phase difference between the OH* emission signal and the pressure from experiments. For both histograms, measurement are performed at 5.5 mm from the injection plan (details may be found in Armbruster et al.[13]). There is a good qualitative agreement between the two figures. The maximum of occurrences is located near zero, indicating in both case a positive coupling between heat release and pressure. Also, a gaussian like distribution is observed for both cases with a comparable standard deviation. This agreement between the two figures suggests the flame response is qualitatively well reproduced in the numerical simulation.

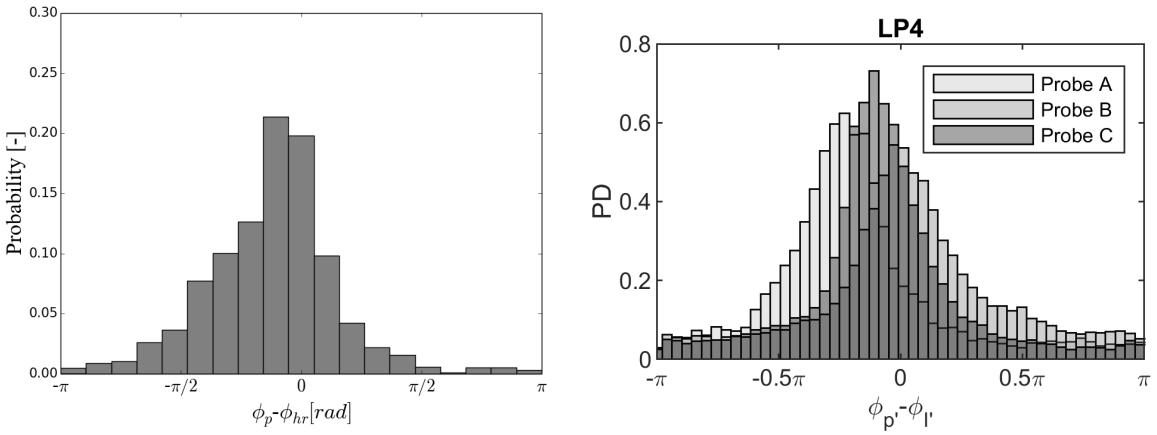

Figure 6: Left: histogram of the phase shift between the pressure and the heat release for the LES of case T131 on mesh M2. Right: histogram of the phase shift between the pressure and OH* emission signal from the experiment for case LP4.[13] Probes A, B and C refer to different azimuthal locations of measurement, see Armbruster et al. for details.[13]

4.4 Conclusions on the impact of the mesh resolution

Main average quantities are found to be weakly dependent on the mesh resolution and even a poorly resolved grid is able to reasonably retrieve the mean fields in the chamber, the eigenmodes frequencies, the pressure loss between the dome and the injector and the heat losses at the walls. However, the pressure dynamics is highly dependent on the grid resolution. Even though the limit cycle amplitude has not been reached, the dynamical behavior obtained in the finest

grid is in good agreement with the experiments. Unfortunately, given the huge amount of CPU ressources needed to compute the final grid, it is not possible to demonstrate a rigorous mesh convergence on the full system, even though the weak sensitivity of the flow field in the near injector region has been checked on a single injector case. Thus, to get more confidence on the predictive capability of the numerical simulations, another injection configuration is computed. This is shown in Sec. 5.

5. Case T65 on mesh M2

The injection conditions of case T131 on mesh M2 is changed to those of case T65 (Tab. 1). As a reminder, only the hydrogen injection temperature is modified, passed from 131 K to 65 K. From the pressure signal of 8 probes in the chamber, the 1T and 2T modes amplitudes are reconstructed following the method depicted in Sliphorst et al.[14] The evolution of these modes in the chamber are plotted in Fig. 7. The initial time corresponds to case T131 on mesh M2. As shown previously, this case features a growing 1T mode and a low amplitude 2T mode. As hydrogen injection temperature is changed to case T65 (dashed line in Fig. 7), the 1T mode amplitude suddenly decreases while the 2T mode presents a rapid augmentation of its amplitude. This behavior is in very good agreement with the experimental observations (Fig. 1b). Even though the limit cycles are not reached, these results are highly encouraging and give a strong confidence on the predictive capability of the numerical methodology.

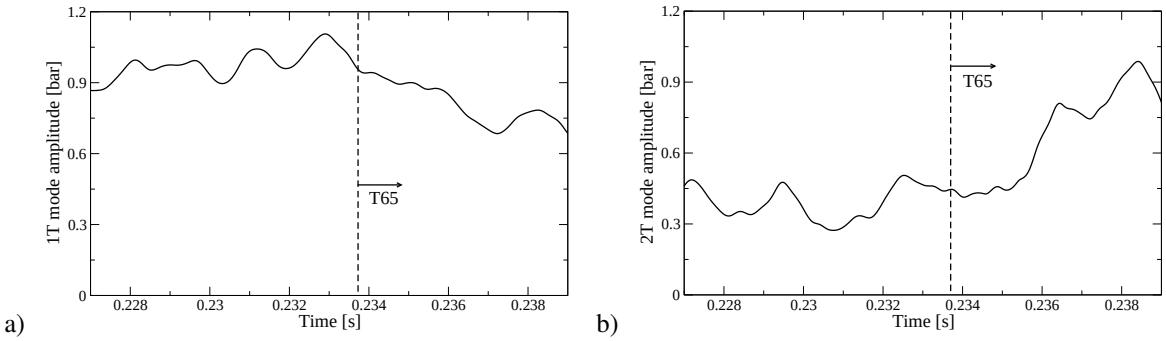

Figure 7: Case T65. Mode amplitude in the chamber. Left: 1T mode amplitude, right: 2T mode amplitude.

The PSD of pressure for case T65 is shown in Fig. 8. The emergence of the 2T mode is confirmed. An important change in the eigenmodes frequencies is noticed: the 1T mode is now at 9 500 Hz and the 2T mode is at 15 300 Hz.

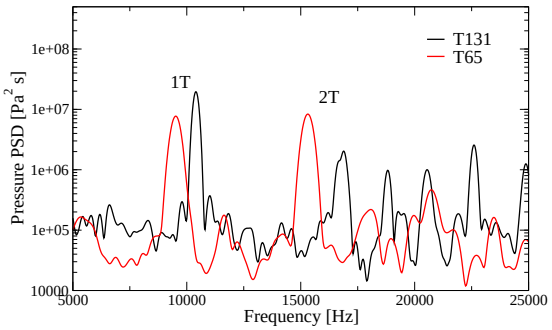

Figure 8: Case T65. Power spectral density of pressure in the chamber for cases T65 and T131 on mesh M2. A Welch's method with 1 block is used, df=200 Hz for case T131 (the last 5 ms are used) and df=310 Hz for case T65 (the last 3 ms are used).

6. Conclusions

Large-Eddy Simulations of the DLR's BKD multi-injector configuration is presented in this paper. The main objective is to assess the impact of the grid resolution on the results. To this respect, 3 different meshes are computed, ranging

from 14 million to 174 million nodes. The main findings are the following:

- The mean and rms profiles of the main flow quantities are very close for the 3 grids, except at the level of the injector exit. As a consequence, this is where most of the mesh refinement occurs.
- The 3 meshes lead to a good prediction of the eigenmode frequencies and the heat losses at the chamber walls.
- Pressure drops between the domes and the chamber are not strongly impacted by the grid refinement.
- The dynamic behavior highly differs between the 3 meshes. In particular, the M0 and M1 meshes predict a dominant mode at 16 kHz (2T mode of the chamber), but with 2 different amplitudes, while the M2 mesh predicts the 1T mode at 10 kHz.
- The finest mesh compares favorably with the experimental measurement in terms of frequency and amplitude of the dominant mode obtained. This has been confirmed simulating another operating point. The change in unstable mode has been captured by the simulation and is in agreement with the experiments.

This study suggests that the finest grid is able to retrieve the instability observed in the experiments. Unfortunately this is at the prize of an important computational cost, out of reach for an actual rocket design study. However, the good prediction of the mean flow variables with the coarse grid is very encouraging and the current results suggest that errors on instability prediction are essentially due to a bad representation of the flow in the recessed part of the injector. Current research thus focuses on the development of dedicated models for this region of the flow.

Acknowledgements

The authors acknowledge PRACE for awarding them access to resource Irene based in France at TGGC (CEA). The support of TGCC (CEA) for access to the computational resources of Irene-Rome under a "grand challenge" allocation is also greatly acknowledged. This work was granted access to the HPC resources of TGCC (CEA), IDRIS and CINES made available by GENCI (Grand Equipement National de Calcul Intensif) under the allocation A0102B06176. A part of this work was performed using HPC resources from the mésocentre computing center of Ecole CentraleSupélec and Ecole Normale Supérieure Paris-Saclay supported by CNRS and Région Ile-de-France.

References

[1] S. Gröning, D. Suslov, J. S. Hardi, and M. Oschwald. Injector-driven combustion instabilities in a hydrogen/oxygen rocket combustor. *Journal of Propulsion and Power*, 32(3):560–573, 2016.

[2] S. Gröning, D. Suslov, J. S. Hardi, and M. Oschwald. Influence of hydrogen temperature on the stability of a rocket engine combustor operated with hydrogen and oxygen. *CEAS Space Journal*, 9:59–76, 2017.

[3] A. Urbano, L. Selle, G. Staffelbach, B. Cuenot, T. Schmitt, S. Ducruix, and S. Candel. Exploration of combustion instability triggering using large eddy simulation of a multiple injector liquid rocket engine. *Combustion and Flame*, 169:129–140, 2016.

[4] A Urbano, Q Douasbin, L Selle, G Staffelbach, B Cuenot, T Schmitt, S Ducruix, and S Candel. Study of flame response to transverse acoustic modes from the les of a 42-injector rocket engine. *Proceedings of the Combustion Institute*, 36(2):2633–2639, 2017.

[5] T. Schmitt, G. Staffelbach, S. Ducruix, S. Gröning, J. Hardi, and M. Oschwald. Large-eddy simulations of a sub-scale liquid rocket combustor: influence of fuel injection temperature on thermo-acoustic stability. In *7TH European Conference for Aeronautics and Aerospace Sciences (EUCASS)*, 2017.

[6] T. Schmitt. Large-eddy simulations of the mascotte test cases operating at supercritical pressure. *Flow, Turbulence and Combustion*, 105:159–189, 2020.

[7] G. Soave. Equilibrium constants from a modified Redlich-Kwong equation of state. *Chemical Engineering Science*, 27:1197–1203, 1977.

[8] B. E. Poling, J. M. Prausnitz, and J. P. O'Connel. *The properties of gases and liquids*. McGraw-Hill, fifth edition, 2001.

[9] F. Nicoud and F. Ducros. Subgrid-scale stress modelling based on the square of the velocity gradient. *Flow, Turbulence and Combustion*, 62(3):183–200, 1999.

[10] O. Colin and M. Rudgyard. Development of high-order Taylor-Galerkin schemes for unsteady calculations. *J. Comput. Phys.*, 162(2):338–371, 2000.

[11] N. Okong'o and J. Bellan. Consistent boundary conditions for multicomponent real gas mixtures based on characteristic waves. *J. Comput. Phys.*, 176:330–344, 2002.

[12] Felix Jaegle, Olivier Cabrit, Simon Mendez, and Thierry Poinsot. Implementation methods of wall functions in cell-vertex numerical solvers. *Flow, turbulence and combustion*, 85(2):245–272, 2010.

[13] Wolfgang Armbruster, Justin S. Hardi, and Michael Oschwald. Flame-acoustic response measurements in a high-pressure, 42-injector, cryogenic rocket thrust chamber. *Proceedings of the Combustion Institute*, 38(4):5963–5970, 2021.

[14] M. Sliphorst, S. Gröning, and M. Oschwald. Theoretical and experimental identification of acoustic spinning mode in a cylindrical combustor. *Journal of Propulsion and Power*, 27(1):182–189, January-February 2011.